

Validation of the CERES Edition 2B Surface-Only Flux Algorithms

DAVID P. KRATZ

Science Directorate, NASA Langley Research Center, Hampton, Virginia

SHASHI K. GUPTA, ANNE C. WILBER, AND VICTOR E. SOTHCOTT

Science Systems Applications, Inc., Hampton, Virginia

(Manuscript received 6 April 2009, in final form 2 July 2009)

ABSTRACT

The Clouds and the Earth's Radiant Energy System (CERES) project uses two shortwave (SW) and two longwave (LW) algorithms to derive surface radiative fluxes on an instantaneous footprint basis from a combination of top-of-atmosphere fluxes, ancillary meteorological data, and retrieved cloud properties. Since the CERES project examines the radiative forcings and feedbacks for Earth's entire climate system, validation of these models for a wide variety of surface conditions is paramount. The present validation effort focuses upon the ability of these surface-only flux algorithms to produce accurate CERES Edition 2B single scanner footprint data from the *Terra* and *Aqua* spacecraft measurements. To facilitate the validation process, high-quality radiometric surface observations have been acquired that were coincident with the CERES-derived surface fluxes. For both SW models, systematic errors range from -20 to -12 W m^{-2} (from -2.8% to -1.6%) for global clear-sky cases, while for the all-sky SW model, the systematic errors range from 14 to 21 W m^{-2} (3.2% – 4.8%) for global cloudy-sky cases. Larger systematic errors were seen for the individual surface types, and significant random errors were observed, especially for cloudy-sky cases. While the SW models nearly achieved the 20 W m^{-2} accuracy requirements established for climate research, further improvements are warranted. For the clear-sky LW model, systematic errors were observed to fall within $\pm 5.4 \text{ W m}^{-2}$ ($\pm 1.9\%$) except for the polar case in which systematic errors on the order from -15 to -11 W m^{-2} (from -13% to -7.2%) occurred. For the all-sky LW model, systematic errors were less than $\pm 9.2 \text{ W m}^{-2}$ ($\pm 7.6\%$) for both the clear-sky and cloudy-sky cases. The random errors were less than 17 W m^{-2} (6.2%) for clear-sky cases and 28 W m^{-2} (13%) for cloudy-sky cases, except for the desert cases in which very high surface skin temperatures caused an overestimation in the model-calculated surface fluxes. Overall, however, the LW models met the accuracy requirements for climate research.

1. Introduction

The shortwave (SW) and longwave (LW) radiative fluxes at the surface are critical components of the surface energy budget, and along with the flows of latent and sensible heat, are as vital to understanding the weather and climate as the SW and LW radiative fluxes at the top of atmosphere (TOA). Obtaining the surface fluxes directly on a global scale, however, is problematic. A viable solution is to derive the surface fluxes from TOA radiance measurements. The Clouds and the Earth's Radiant Energy System (CERES) satellite instrument, as part of the National Aeronautics and Space Administra-

tion (NASA) Earth Observing System (EOS), measures broadband TOA radiances using a scanning radiometer composed of three channels: total ($0.2\text{--}100 \mu\text{m}$), SW ($0.2\text{--}5 \mu\text{m}$), and LW windows ($8\text{--}12 \mu\text{m}$). The CERES project uses the TOA radiance measurements to examine the role of cloud/radiation feedbacks in the earth's climate system and to derive radiant energy quantities for climate data records (Wielicki et al. 1996). Within the CERES processing effort, the TOA radiances are converted into TOA fluxes through the use of angular distribution models (Loeb et al. 2005, 2007) that were formulated primarily for use in the processing of the CERES measurements. The TOA fluxes along with ancillary meteorological data and cloud property retrievals (Minnis et al. 1997) are then incorporated into the CERES processing stream to estimate radiative fluxes at the surface and at several levels within the

Corresponding author address: Dr. David P. Kratz, NASA Langley Research Center, Mail Stop 420, Hampton, VA 23681-2199.
E-mail: david.p.kratz@nasa.gov

atmosphere. These single scanner footprint-level fluxes are then gridded and time averaged to produce global climate data records (Young et al. 1998). The present paper is concerned with the algorithms that are used to derive the surface-only fluxes on the single scanner footprint level.

The CERES project incorporates two SW and two LW surface-only flux algorithms (SOFA) to retrieve surface fluxes directly from TOA measurements. Based upon rapid radiative transfer parameterizations, the SOFA models have undergone extensive validation, intercomparison, and improvement as part of the CERES endeavor. The use of algorithms that were formulated using very different approaches has allowed for independent intercomparisons and analyses of both the SW and LW results. The SOFA models have also been used to examine the accuracy of the more comprehensive Surface and Atmospheric Radiation Budget (SARB) algorithms (Charlock et al. 1997, 2006), which are based upon complex physical models requiring detailed knowledge of the atmospheric state. Since the SOFA models rely upon relatively simple parameterizations, the formulations are not as precisely defined as those obtained from detailed physical algorithms; however, the speed and ability to produce accurate results of the SOFA models have demonstrated their usefulness.

Because the original formulations for the two SW and two LW SOFA models were written in vastly different styles, for clarity, section 2 presents the models using formulations that are mutually consistent. Section 3 provides a brief discussion of the surface data used to validate the models. Section 4 follows with a detailed discussion of the validation and intercomparison studies. Summaries of the validation methods along with the results from this study are presented in section 5.

2. Surface flux models

a. SW models

1) SW MODEL A

Li et al. (1993b) applied radiative transfer calculations to an extensive set of surface and atmospheric conditions to derive a linear parameterization capable of estimating the net SW surface flux $F_{0,S}^{\text{net}}$ in terms of the solar constant S_0 , normalized Earth–sun distance d , TOA albedo α_{toa} , column water vapor amount w , cosine of the solar zenith angle μ , and several regression coefficients. For simplicity, this formulation can be summarized as

$$F_{0,S}^{\text{net}} = S_0 d^{-2} \mu [A(\mu, w) - B(\mu, w) \alpha_{\text{toa}}], \quad (1)$$

where the functions, $A(\mu, w)$ and $B(\mu, w)$, represent the intercept and slope coefficients determined by linear

regression analysis. A standard textbook procedure (e.g., Peixoto and Oort 1993) is used to calculate the instantaneous values for the downward SW TOA flux $F_{\text{toa},S}^- = S_0 d^{-2} \mu$ for daytime cases where $\mu \geq 0$. Although Li et al. (1993b) derived intercept and slope coefficients for a variety of sky conditions, a follow-up study by Li et al. (1993a) reported that the clear-sky coefficients provided satisfactory results regardless of cloud type or cloud cover amount. Thus, the CERES processing effort has followed the recommendation of Li et al. (1993a) and used the clear-sky coefficients with the parameterization. To improve upon the basic aerosol term in the Li et al. (1993b) algorithm, however, SW model A has included the aerosol correction term derived by Masuda et al. (1995).

Net fluxes are of particular interest in climate analysis studies since they quantify the energy budget at any location within the earth's atmosphere system (Li et al. 1993b). The limited availability of net fluxes from ground-based measurements, however, has hindered efforts to validate net fluxes derived from the satellite data. As an alternative, validation studies have relied on more prevalent measurements of the downward fluxes at the surface, thus providing more extensive validation opportunities.

If the surface albedo α_0 is available, the downward SW surface flux $F_{0,S}^-$ can be calculated from the net surface flux using

$$F_{0,S}^- = \frac{F_{0,S}^{\text{net}}}{(1 - \alpha_0)}. \quad (2)$$

Li and Garand (1994) created a surface albedo parameterization for use with the Li et al. (1993b) algorithm by using five years of Earth Radiation Budget Experiment (ERBE) clear-sky satellite data (Barkstrom et al. 1989). While preliminary validation studies showed good results for clear-sky conditions, very large data scatter for cloudy-sky conditions suggested that the Li and Garand (1994) surface albedo maps were not appropriate for cloudy-sky conditions. As a consequence, SW model A has only been run in clear-sky mode for the CERES processing.

2) SW MODEL B

The second SW model, the Langley parameterized shortwave algorithm (LPSA), relies upon simple physical relationships to estimate the attenuation of the SW radiation by the earth's atmosphere for both clear- and cloudy-sky conditions (Gupta et al. 2001). In this algorithm, the downward SW surface flux $F_{0,S}^-$ is defined for daytime cases to be

$$F_{0,S}^- = S_0 d^{-2} \mu T_a T_c, \quad (3)$$

where T_a represents the transmittance of the clear atmosphere, and T_c represents the transmittance of the clouds (Darnell et al. 1988, 1992). Combining Eqs. (2) and (3) results in an equation for $F_{0,S}^{\text{net}}$ that is similar to Eq. (1) with the all-important difference that SW model B uses the surface albedo to derive $F_{0,S}^{\text{net}}$ from $F_{0,S}^-$, whereas SW model A derives $F_{0,S}^{\text{net}}$ directly. In addition, there are significant differences between these models concerning the calculation of the transmittance along the path. Specifically, the clear-sky transmittance in SW model B is determined by

$$T_a = (1 + B) \exp(-\tau_z), \quad (4)$$

where B represents the scattering of surface-reflected radiation by the atmosphere (gases and aerosols), and τ_z is the broadband extinction optical depth at solar zenith angle z that accounts for absorption and backscattering in the clear atmosphere. Cloud transmittance is computed using a threshold method (see Darnell et al. 1992) given by

$$T_c = 0.05 + 0.95 \frac{(R_{\text{ovc}} - R_{\text{meas}})}{(R_{\text{ovc}} - R_{\text{clr}})}, \quad (5)$$

where R_{ovc} , R_{clr} , and R_{meas} represent values of overcast, clear, and instantaneously measured TOA reflectances, respectively, for the CERES footprint. Equation (5) is based on standard threshold methods used for cloud parameter determination (e.g., Moser and Raschke 1984) as well as the recognition that even the thickest clouds do not reduce T_c to zero. The values of R_{ovc} were computed using an empirical relation developed from the International Satellite Cloud Climatology Project (ISCCP; Rossow and Schiffer 1999) data. The values of R_{clr} were developed from the monthly clear-sky reflectance climatologies using the existing 48 months of ERBE data for *Terra* and 46 months of the CERES data, taken aboard the *Terra* satellite, for *Aqua*. Future editions of CERES processing for both *Terra* and *Aqua* will only use R_{clr} values developed from the CERES data. A more comprehensive discussion of the LPSA is available in Gupta et al. (2001).

b. LW models

1) LW MODEL A

Inamdar and Ramanathan (1997) created an analytical technique to compute the downward LW surface flux $F_{0,L}^-$ from the sum of the downward LW window surface flux $F_{0,L,\text{win}}^-$ and the LW nonwindow surface flux $F_{0,L,\text{nw}}^-$:

$$F_{0,L}^- = F_{0,L,\text{win}}^- + F_{0,L,\text{nw}}^- \quad (6)$$

Such an algorithm takes advantage of the physical differences between the spectral range for the infrared window (8–12 μm) where satellite instruments can directly sense the surface for clear-sky conditions and the spectral range for the nonwindow where the TOA and surface fluxes are essentially decoupled.

For the window region, Inamdar and Ramanathan (1997) found that the energetics of the system could best be described in terms of the upward LW window surface flux $F_{0,L,\text{win}}^+$, the upward LW window TOA flux $F_{\text{toa},L,\text{win}}^+$, w , the air temperature θ_a , a quantity determined at pressure P_e defined by $P_e = (P_s/2000.0 + 0.45)P_s$, where P_s is the surface pressure (hPa), and the near-surface air temperature θ_0 , a quantity that for most cases is equivalent to the surface skin temperature (S. K. Gupta et al. 2009, unpublished manuscript, hereinafter GKSW). Since the atmospheric absorption due to water vapor does not saturate in the window region, emission to the surface could be expressed as a linear term in w , in combination with temperature and optical depth. Furthermore, since the transmittance in the window region is nearly exponential, the ratio $F_{\text{toa},L,\text{win}}^+/F_{0,L,\text{win}}^+$ is a good approximation for the optical depth (Inamdar and Ramanathan 1997). Thus, the downward LW flux to the surface in the window region has been expressed as

$$F_{0,L,\text{win}}^- = c_1(F_{0,L,\text{win}}^+ - F_{\text{toa},L,\text{win}}^+) + \left[c_2 w + c_3 \ln\left(\frac{F_{\text{toa},L,\text{win}}^+}{F_{0,L,\text{win}}^+}\right) + c_4 \theta_0 + c_5 \theta_a \right] F_{\text{toa},L,\text{win}}^+ + c_6 F_{0,L}^+, \quad (7)$$

where c_1 – c_6 are determined through regression analyses and vary with geographical region.

For the nonwindow region, Inamdar and Ramanathan (1997) found that the principal variables were the upward LW nonwindow surface flux $F_{0,L,\text{nw}}^+$, the upward LW nonwindow TOA flux $F_{\text{toa},L,\text{nw}}^+$, $\ln(w)$, θ_a , and θ_0 . Unlike the window region, the water vapor absorption in the pure-rotation and rotation–vibration bands in the nonwindow regions tends to be in the logarithmic limit (Cess and Tiwari 1972), and hence, the emission to the surface should be expressed as a logarithmic function of w . Thus, the downward LW flux to the surface in the nonwindow region has been expressed as

$$F_{0,L,\text{nw}}^- = c_7(F_{0,L,\text{nw}}^+ - F_{\text{toa},L,\text{nw}}^+) + [c_8 \ln(w) + c_9 \theta_0 + c_{10} \theta_a] F_{\text{toa},L,\text{nw}}^+ + c_{11} F_{0,L}^+, \quad (8)$$

where c_7 – c_{11} are determined through regression analyses and vary with geographical region. A recent study

by Zhou et al. (2007) has demonstrated, however, that algorithms formulated in terms of $\ln(w)$ can severely underestimate the downward LW flux for cases involving low water vapor amounts, $w < 1$ cm, thereby leading to significant errors for high-altitude and high-latitude regions. A viable solution is to reformulate such algorithms in terms of $\ln(1 + w)$, which retains the logarithmic limit for large values of w but asymptotes to the linear limit as w approaches zero.

Inamdar and Ramanathan (1997) refer to the difference between the upward surface and TOA fluxes found in the first terms of Eqs. (7) and (8) as the clear-sky greenhouse effect of the atmosphere for the window and nonwindow regions, respectively. Their observation that the greenhouse effect of the atmosphere was highly correlated to the emission to the surface led Inamdar and Ramanathan (1997) to the formulations given by Eqs. (7) and (8). The trailing terms in Eqs. (7) and (8), which are proportional to the upward broadband surface flux, $F_{0,L}^+$, are merely the result of intercept offsets from their regression analysis.

2) LW MODEL B

LW model B uses the Langley parameterized long-wave algorithm (LPLA) that was developed from an accurate narrowband radiative transfer model (Gupta 1989; Gupta et al. 1992) using an extensive meteorological database of satellite and in situ measurements to provide the capability of rapidly computing the downward, upward, and net LW radiative fluxes at the earth's surface for both clear- and cloudy-sky conditions. To calculate the downward LW surface flux, $F_{0,L}^-$, LW model B first calculates the downward clear-sky LW surface flux, $F_{0,L,\text{clr}}^-$, using a functional dependence on column water vapor, $g(w)$, and an effective emitting temperature, θ_e , for the lower atmosphere:

$$F_{0,L,\text{clr}}^- = g(w)\theta_e^{3.7}. \quad (9)$$

For this model, the effective emitting temperature for the lower atmosphere is derived using a weighted average of the temperatures of the lower-tropospheric layers, θ_1 and θ_2 , and the near-surface air temperature, θ_0 :

$$\theta_e = 0.60\theta_0 + 0.35\theta_1 + 0.05\theta_2. \quad (10)$$

LW model B then calculates the downward cloudy-sky LW surface flux $F_{0,L,\text{cld}}^-$ using the cloud-base height and temperature as well as the column water vapor amount below the cloud base. Combining the clear- and cloudy-sky results, along with the fractional cloudy-sky amount, f_{cld} , allows for the calculation of the downward LW surface flux:

$$F_{0,L}^- = F_{0,L,\text{clr}}^- + (F_{0,L,\text{cld}}^- - F_{0,L,\text{clr}}^-)f_{\text{cld}}. \quad (11)$$

Taking the partial derivative of $F_{0,L}^-$ with respect to f_{cld} yields $\partial F_{0,L}^- / \partial f_{\text{cld}} = F_{0,L,\text{cld}}^- - F_{0,L,\text{clr}}^-$, indicating that the difference between the downward clear- and cloudy-sky surface fluxes represents the sensitivity of the downward cloudy-sky surface flux to the fractional cloudy-sky amount. By incorporating surface emissivity maps (Wilber et al. 1999), the upward and net fluxes can then be calculated from the downward fluxes.

c. Input data

The input parameters necessary to run the SW and LW models have been obtained from various sources available in the CERES processing stream. Humidity and temperature profiles are archived in the Meteorology, Ozone, and Aerosol (MOA) database (Gupta et al. 1997). For the CERES Edition 2B processing, the MOA profiles were created from a static data assimilation product obtained from the Global Modeling and Assimilation Office (GMAO) Goddard Earth Observing System (GEOS), version 4.0.3 (Bloom et al. 2005), dataset and the National Centers for Environmental Prediction–Stratosphere Monitoring Ozone Blended Analysis (NCEP–SMOBA) ozone products (Yang et al. 1997). Fractional cloud amount and cloud-base height were available for flux computations from the cloud subsystem within the CERES processing (Minnis et al. 1997) where the cloud properties were derived using high-resolution imager data (Salomonson et al. 1989) from the Moderate Resolution Imaging Spectroradiometer (MODIS) flown aboard the *Terra* and *Aqua* satellites. The TOA fluxes were available from the CERES inversion subsystem.

3. Surface validation data

Prior to the availability of high-quality surface flux measurements, validation studies compared the empirical and statistical parameterizations to physical radiative transfer algorithms through the auspices of such endeavors as the Intercomparison of Radiation Codes in Climate Models (ICRCCM) program (Ellingson et al. 1991). While extremely valuable for ascertaining the accuracy of the parameterized models under controlled conditions, such comparisons do not provide reliable estimates of the accuracies of retrieved surface fluxes under operational conditions. In the 1990s, the introduction of reliable ground-based programs to measure surface fluxes allowed for more realistic comparisons to be undertaken. Indeed, since that time, high-quality radiometric observations have become available at many locations around the world. The CERES/SARB working

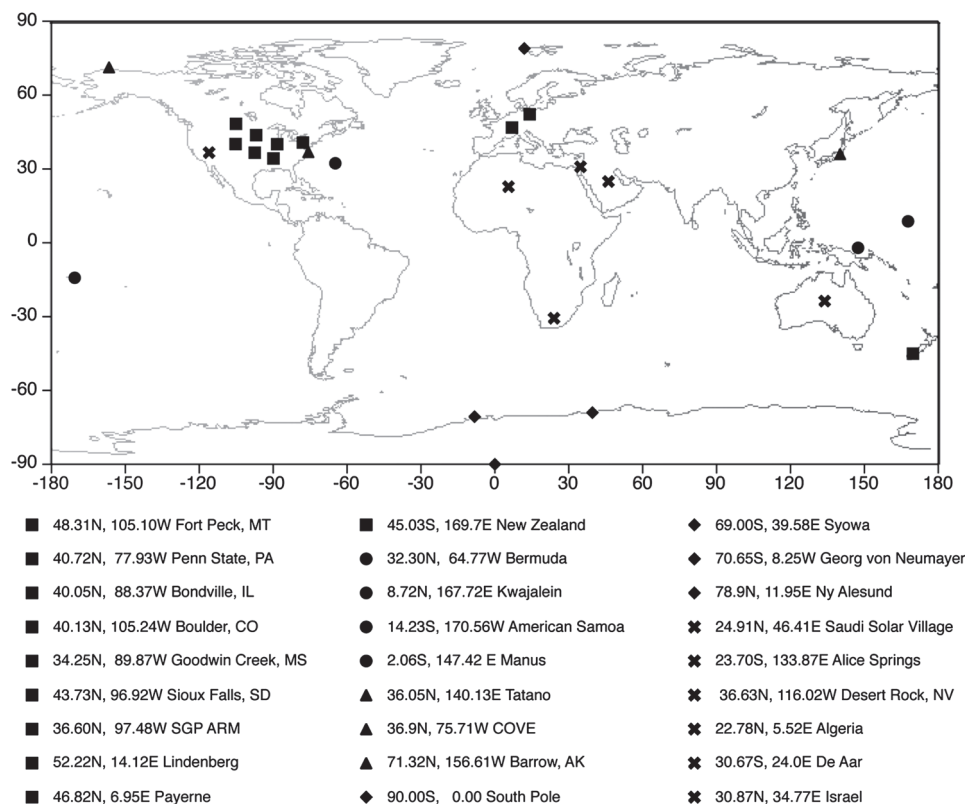


FIG. 1. Locations of the surface sites used in this study. The different symbols represent the different surface types as follows: continental (square), island (circle), coastal (triangle), polar (diamond), and desert (x).

group has assembled the surface flux measurements into a database primarily intended for CERES validation studies (Rutan et al. 2001), but has since made the data freely available to the worldwide science community [through the NASA Langley Research Center (LaRC) CERES/Atmospheric Radiation Measurement Program (ARM) Validation Experiment (CAVE) online at <http://www-cave.larc.nasa.gov/cave/>]. All surface sites in the CAVE database adhere to the stringent accuracy and calibration requirements set forth by the Baseline Surface Radiation Network (BSRN).

This study incorporated broadband surface measurements obtained from the CAVE Web site for seven of the U.S. Department of Energy (DOE) ARM sites, including five in the southern Great Plains (SGP) network and two in the tropical western Pacific (TWP) network (Stokes and Schwartz 1994); 13 Global Monitoring Division (GMD) sites, seven of which are part of the Surface Radiation Budget Network (SURFRAD) in the continental United States (Augustine et al. 2000); 12 international BSRN sites (Ohmura et al. 1998); and the CERES Ocean Validation Experiment (COVE) site (Jin et al. 2002). The surface sites for this study were

selected on the basis of data availability as well as their ability to represent different surface types (e.g., island, coastal, polar, continental, and desert). The locations of the surface sites used in this study are presented in Fig. 1. Temporal matching between the satellite and surface site fluxes was determined by the highest temporal resolution available from the surface site data, which for most surface sites in this study is 1 min. Spatial matching between the satellite and surface fluxes was determined by the half-width of the nadir-viewing footprint. At an altitude of approximately 700 km for the *Terra* and *Aqua* satellites, the nominal size of the CERES instrument nadir-viewing footprint is 20 km. Thus, to facilitate the intercomparison of satellite and surface fluxes, the fluxes derived from the CERES measurements were averaged together for all footprints located within 1 min of the time of the surface measurement and 10 km of the surface site.

Most surface validation sites use two techniques to obtain the surface insolation. The first technique derives the downward SW surface flux by using a normal incidence pyrheliometer (NIP) to measure the direct solar irradiance along with a shaded pyranometer to measure

the diffuse SW flux over the remainder of the hemispherical solid angle. If the tracking capabilities of the two instruments are reliable, this technique provides the highest accuracies, especially for clear-sky conditions (Michalsky et al. 1999), but only if proper care is exercised to account for thermal offsets (Philipona 2002). Consequently, the reliability of this technique requires a fairly high degree of monitoring and maintenance. Indeed, an earlier study (Gupta et al. 2004) found that during the time when the CERES instrument was operational aboard the Tropical Rainfall Measuring Mission (TRMM), the insolation data records produced by this instrument combination were plagued by large discrepancies and frequent data gaps, many of which could be traced back to malfunctions in the solar tracking components. Thus, there is a need for a viable alternative whenever tracking anomalies occur with either the NIP or shaded pyranometer measurements. Such an alternative technique is available through the use of unshaded pyranometers, which measure the downward SW surface flux directly from the entire sky. Since an unshaded pyranometer has no moving parts, there are no tracking errors, and not surprisingly there is a tendency to produce considerably fewer data gaps. The unshaded pyranometer, however, is subject to cosine errors (Augustine et al. 2000), and since such devices are calibrated to measurements taken within the range of solar zenith angles from 45° to 55° , the insolation retrievals tend to be overestimated at low solar zenith angles and underestimated at high solar zenith angles (Augustine et al. 2000). Despite the cosine errors, for cloudy-sky conditions the unshaded pyranometer measurements have been found to be nearly as accurate as the combined NIP and shaded pyranometer measurements (Gupta et al. 2004). Thus, for the production of the GMD surface flux datasets, quality control methods have been applied to harvest the most reliable insolation measurements taken by these two separate techniques (E. Dutton 2003, personal communication). In an effort to have the best possible validation datasets, similar quality control analyses have also been applied at LaRC to the other ground-truth measurements. In contrast with the SW instruments, the pyrgeometers used to measure the downward LW surface fluxes exhibited no obvious problems at any of the surface sites.

4. Validation results

Comparing the SW and LW Edition 2B surface fluxes with the surface validation measurements has tested the accuracy and precision of the CERES surface-only flux algorithms. The Edition 2B surface fluxes were derived from the *Terra* measurements during the 77-month pe-

riod from March 2000 through July 2006 and from the *Aqua* measurements during the 46-month period from July 2002 through April 2006. The timeframe of CERES Edition 2B coincides with the MODIS Collection-4 data production, which allows for a consistent multiyear data record. CERES data processing after this time uses a different MODIS data collection. Although the CERES instruments aboard both the *Terra* and *Aqua* satellites are capable of various tracking modes, only the CERES cross-track data have been used in the present validation study. As per the recommendation of Gupta et al. (2004), surface site measurements are averaged over 1 min for the clear-sky SW, clear-sky LW, and cloudy-sky LW, and over 60 min for the cloudy-sky SW. To avoid ambiguity in the sign of the fluxes, the CERES project has defined all fluxes into the surface as being positive and all fluxes leaving the surface as being negative. Thus, a positive net flux at the surface indicates warming while a negative net flux indicates cooling.

a. SW models

Statistical comparisons between the CERES-derived and surface-measured downward SW fluxes are presented in Table 1 for both the *Terra* and *Aqua* orbital crossings over the 33 surface sites considered in this study. Percentage differences are provided in addition to the flux values for the systematic and random errors in Table 1 to gauge the relative importance of the flux values. For brevity, the comparisons are arranged by surface type—*island, coastal, polar, continental, desert, and global*—rather than by individual surface site. The global surface type merely represents the combination of all the other surface types. Graphical comparisons for the *Aqua* overpasses are shown in Fig. 2. The corresponding results for the *Terra* overpasses have not been presented since the *Terra* and *Aqua* comparisons are very similar for most of the cases in this study. The only exceptions are two polar surface sites, to be discussed later, where a modification of an input parameter for SW model B significantly improved the cloudy-sky results for *Aqua* as compared with *Terra*.

Figure 2a and the top portion of Table 1 show the clear-sky comparisons between SW model A and the surface measured results. Figure 2b shows the corresponding comparisons for the bin-averaged data, which reveals the overall relationship obscured by the sampling noise. The global comparisons reveal that the surface fluxes derived using SW model A have modest negative systematic errors from -18 to -12 W m^{-2} and random errors from 41 to 46 W m^{-2} . The polar cases that dominate fluxes of $<500 \text{ W m}^{-2}$, however, show a persistent average systematic error from -53 to -46 W m^{-2} . This, in combination with the continental cases, which show

TABLE 1. Comparisons between surface-measured fluxes and CERES-derived fluxes for SW model A under clear-sky conditions, SW model B under clear-sky conditions, and SW model B under cloudy-sky conditions for a variety of scene types. The columns represent the surface type (Type), the number of measurements (n), the mean value of the CERES-derived fluxes (Mean), the systematic errors (CERES derived – surface measured; Bias), and the random errors (σ). For the systematic and random errors, percentage differences are provided in parentheses in addition to the flux values.

Type	Terra 2B SW model A clear sky				Aqua 2B SW model A clear sky			
	n	Mean $W\ m^{-2}$	Bias $W\ m^{-2}$ (%)	$\sigma\ W\ m^{-2}$ (%)	n	Mean $W\ m^{-2}$	Bias $W\ m^{-2}$ (%)	$\sigma\ W\ m^{-2}$ (%)
Island	101	932.7	32.9 (3.7)	56.6 (6.3)	43	899.6	43.3 (5.1)	69.6 (8.1)
Coastal	286	682.4	7.7 (1.1)	31.0 (4.6)	149	680.2	–0.1 (–0.0)	26.9 (4.0)
Polar	540	359.8	–53.1 (–12.9)	24.6 (5.9)	349	379.8	–46.1 (–10.8)	23.6 (5.5)
Continental	3156	727.8	–5.3 (–0.7)	31.7 (4.3)	1394	691.5	–11.2 (–1.6)	30.6 (4.4)
Desert	2117	823.0	–16.1 (–1.9)	39.3 (4.7)	620	789.5	–27.3 (–3.3)	58.3 (7.1)
Global	6200	729.5	–11.9 (–1.6)	41.7 (5.6)	2555	675.6	–18.3 (–2.6)	45.7 (6.6)

Type	Terra 2B SW model B clear sky				Aqua 2B SW model B clear sky			
	n	Mean $W\ m^{-2}$	Bias $W\ m^{-2}$ (%)	$\sigma\ W\ m^{-2}$ (%)	n	Mean $W\ m^{-2}$	Bias $W\ m^{-2}$ (%)	$\sigma\ W\ m^{-2}$ (%)
Island	105	917.3	15.2 (1.7)	53.0 (5.9)	43	882.4	26.0 (3.1)	66.8 (7.8)
Coastal	289	659.4	–13.7 (–2.0)	26.7 (4.0)	151	676.8	–4.5 (–0.7)	24.8 (3.6)
Polar	585	387.9	–2.9 (–0.7)	15.9 (4.1)	362	416.1	–2.4 (–0.6)	14.0 (3.3)
Continental	3163	711.2	–21.8 (–3.0)	28.3 (3.9)	1401	678.8	–23.8 (–3.4)	27.9 (4.0)
Desert	2117	815.2	–23.9 (–2.9)	40.6 (4.8)	624	786.5	–29.9 (–3.7)	41.9 (5.1)
Global	6259	717.2	–19.8 (–2.7)	36.9 (5.0)	2581	671.3	–20.3 (–2.9)	35.3 (5.1)

Type	Terra 2B SW model B cloudy-sky hour				Aqua 2B SW model B cloudy-sky hour			
	n	Mean $W\ m^{-2}$	Bias $W\ m^{-2}$ (%)	$\sigma\ W\ m^{-2}$ (%)	n	Mean $W\ m^{-2}$	Bias $W\ m^{-2}$ (%)	$\sigma\ W\ m^{-2}$ (%)
Island	4776	716.7	56.2 (8.5)	100.2 (15.2)	2974	683.0	54.3 (8.6)	103.2 (16.4)
Coastal	1846	541.0	36.1 (7.1)	66.7 (13.2)	1294	542.9	38.1 (7.5)	68.3 (13.5)
Polar	14 125	237.1	–12.8 (–5.1)	94.0 (37.6)	8701	259.0	9.5 (3.8)	71.3 (28.6)
Continental	10 343	528.7	30.8 (6.2)	100.9 (20.3)	6919	519.4	27.3 (5.5)	80.9 (16.4)
Desert	2540	595.7	–4.1 (–0.7)	102.7 (17.1)	2467	644.0	–5.6 (–0.9)	88.0 (13.5)
Global	33 630	438.7	13.8 (3.2)	107.9 (25.4)	22 355	454.9	21.0 (4.8)	87.1 (20.1)

similar negative systematic errors below $500\ W\ m^{-2}$ for the high-latitude wintertime conditions, as well as the lack of corresponding negative systematic errors in the available net flux comparisons, suggests that the source of this underestimation is the Li and Garand (1994) surface albedo formulation, which is based on a surface albedo climatology that excluded polar areas. The desert cases show a modest negative systematic error for values below $800\ W\ m^{-2}$; however, above that value, the desert cases show a large negative systematic error exceeding $50\ W\ m^{-2}$ that results in increased overall bias and scatter. An unambiguous cause has not been found to explain this large negative systematic error in the desert retrievals. The small number of outliers that severely overestimate the flux in Fig. 2a have been linked to scenes that have been classified as being clear for CERES processing, even though close examination of the surface measurements has demonstrated that the surface measurements are being affected by transient cumulus clouds.

Figures 2c and 2d and the middle portion of Table 1 show the clear-sky comparisons between SW model B and the surface-measured results. The global compari-

sons reveal that the surface fluxes derived using SW model B have modest negative systematic errors of the order $-20\ W\ m^{-2}$ and random errors of the order $35\ W\ m^{-2}$. Although the statistical results for the global clear-sky comparisons for SW model B are similar to those produced by SW model A, there are notable differences for the various scene types. Foremost are the polar cases where SW model B has shown an ability to produce surface fluxes that are in excellent agreement with the surface measured fluxes, with systematic errors smaller than $-5\ W\ m^{-2}$ and random errors of the order $15\ W\ m^{-2}$. The continental and desert cases, however, show persistent systematic errors from -30 to $-20\ W\ m^{-2}$ throughout the entire range of measurements, which contrasts with SW model A where such negative systematic errors tend to occur only below $500\ W\ m^{-2}$ for the continental cases and above $800\ W\ m^{-2}$ for the desert cases. SW model B systematic errors for the island and coastal cases also tend to be 5 – $20\ W\ m^{-2}$ lower than the SW model A systematic errors. As before, the same points that produced severe overestimations of the flux in Fig. 2a for SW model A also

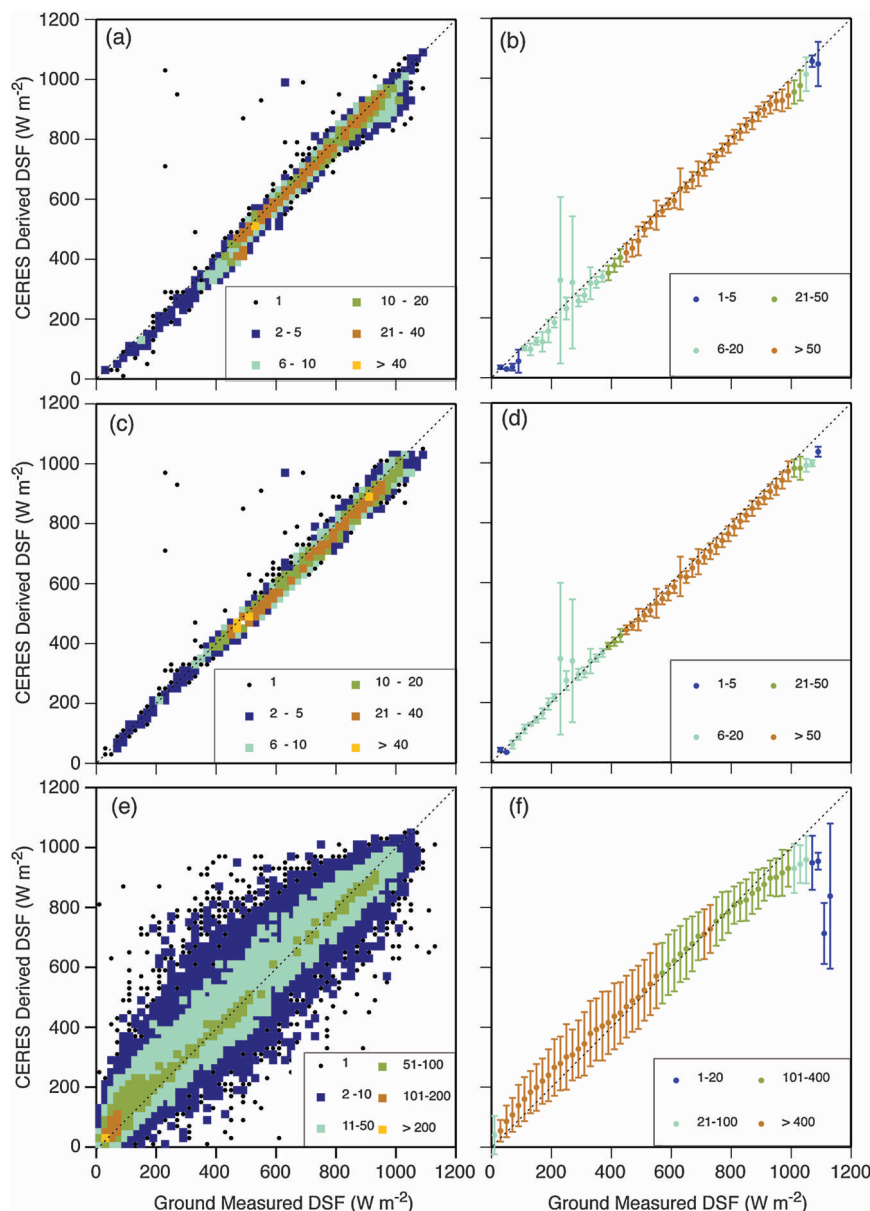


FIG. 2. Graphical comparisons between surface-measured fluxes and CERES-derived fluxes from *Aqua* measurements for (a),(b) SW model A under clear-sky conditions, (c),(d) SW model B under clear-sky conditions, and (e),(f) SW model B under cloudy-sky conditions for all the surface sites used in this study. Panels (a),(c), and (e) represent 2D histograms that illustrate the number of coincident flux values found within each 20 W m^{-2} square bin; (b),(d), and (f) represent the mean and standard deviation of the CERES-derived fluxes found within each 20 W m^{-2} bin of surface-measured fluxes. The legends define the number of values in each bin.

produce severe overestimations of the flux in Fig. 2b for SW model B, further supporting the conclusion that these points have been misclassified as being clear.

Figures 2e and 2f and the lower portion of Table 1 show the cloudy-sky comparisons between SW model B and the surface-measured results. Because the spatial variability within cloud fields frequently produces con-

ditions where 1-min averaging of the surface measurements is not representative of surface conditions over the entire 20-km CERES footprint, this study has instead compared CERES-derived surface fluxes for cloudy skies to the 60-min averaged surface measurements. Even though such 60-min averaged surface measurements are considered optimal (Gupta et al. 2004), there remains

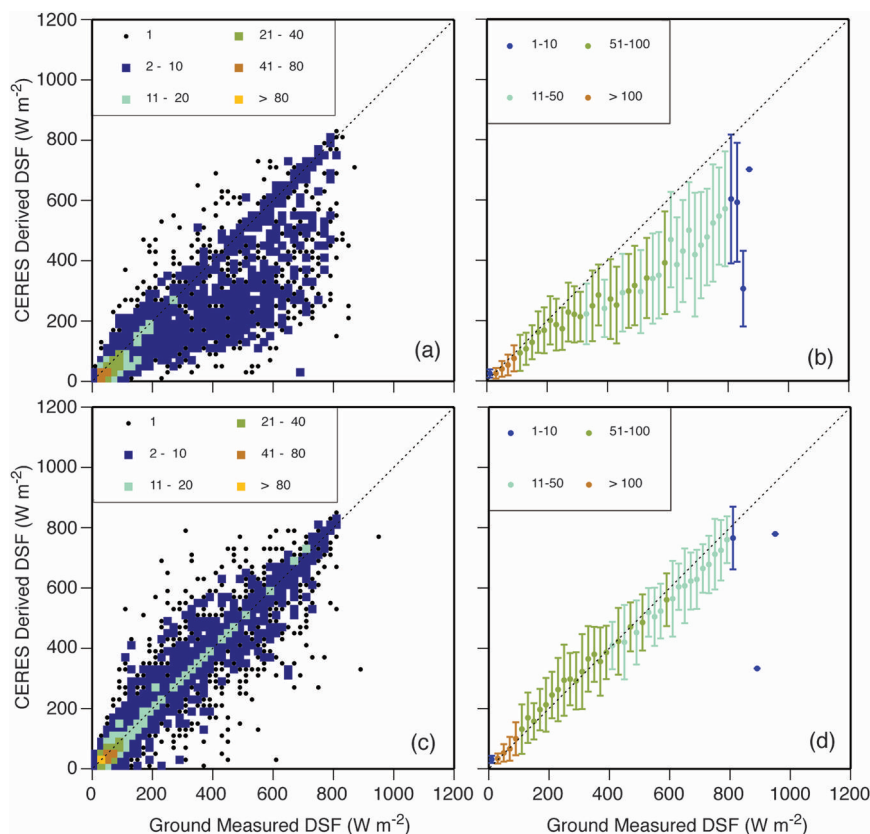


FIG. 3. Graphical comparisons between surface-measured fluxes and CERES-derived fluxes for SW model B under cloudy-sky conditions for the polar sites Georg von Neumayer and Syowa showing the improvement between the (a),(b) *Terra* and (c),(d) *Aqua* measurements. Panels (a) and (c) represent 2D histograms that illustrate the number of coincident flux values found within each 20 W m^{-2} square bin. Panels (b) and (d) represent the mean and standard deviation of the CERES-derived fluxes found within each 20 W m^{-2} bin of surface-measured fluxes. The legends define the number of values in each bin.

considerable scatter in the comparisons, greater than 105 W m^{-2} for *Terra* and 85 W m^{-2} for *Aqua*. These results are consistent with other studies (e.g., Rossow and Zhang 1995; Gautier and Landsfeld 1997) where random errors of similar magnitude have also been observed for the cloudy-sky cases. Because satellite and surface instruments measure significantly different conical sections of the sky, these two viewpoints sense very different spatial distributions of clouds, and therefore, even optimizing the averaging times, the random errors tend to be larger for cloudy-sky comparisons than for the more homogeneous clear-sky comparisons. Despite the large random errors, the systematic errors for the global cases are of the order 14 W m^{-2} for *Terra* and 21 W m^{-2} for *Aqua*, with the difference between *Terra* and *Aqua* being almost entirely due to the polar cases. The cause for this difference is discussed in detail in the next paragraph.

As noted previously, most of the comparisons between the CERES-derived and the surface-measured

SW fluxes produce similar results for *Terra* and *Aqua*. The only notable exceptions are the cloudy-sky cases for the polar surface sites Georg von Neumayer and Syowa where significant differences occur between the results from *Terra* in Figs. 3a and 3b and *Aqua* in Figs. 3c and 3d. The plots for *Terra* show a very poor correlation with a large negative bias, which has been attributed to the inadequacies in the monthly climatological ERBE clear-sky TOA albedos. In contrast, the plots for *Aqua* show comparisons that are reasonably well correlated with a modest bias, though there does remain a large scatter. This improvement in the *Aqua* processing is due to the use of a much-improved TOA albedo dataset derived from 46 months of *Terra* data. Even though the *Aqua* processing has resulted in significant improvements in the cloudy-sky results for the Georg von Neumayer and Syowa surface sites, the global bias was increased because of the elimination of the compensating negative systematic errors from these polar sites. The observation

TABLE 2. Comparisons between surface-measured fluxes and CERES-derived fluxes for LW model A under clear-sky conditions, LW model B under clear-sky conditions, and LW model B under cloudy-sky conditions for a variety of scene types. The column format is the same as Table 1.

Terra 2B LW model A clear sky					Aqua 2B LW model A clear sky			
Type	<i>n</i>	Mean W m ^{−2}	Bias W m ^{−2} (%)	σ W m ^{−2} (%)	<i>n</i>	Mean W m ^{−2}	Bias W m ^{−2} (%)	σ W m ^{−2} (%)
Island	263	394.0	−0.4 (−0.1)	10.9 (2.8)	118	389.8	0.3 (0.1)	11.6 (3.0)
Coastal	804	284.9	2.8 (1.0)	12.8 (4.5)	501	287.4	4.3 (1.5)	12.8 (4.5)
Polar	781	142.2	−11.1 (−7.2)	15.3 (10.0)	996	103.3	−15.2 (−12.8)	12.9 (10.9)
Continental	6798	294.6	−3.5 (−1.2)	13.1 (4.4)	3682	281.8	−5.4 (−1.9)	13.4 (4.7)
Desert	4375	318.8	4.3 (1.4)	20.9 (6.7)	1771	305.1	1.0 (0.3)	24.6 (8.1)
Global	13 021	295.0	−0.9 (−0.3)	16.9 (5.7)	7068	264.7	−4.4 (−1.6)	17.6 (6.5)

Terra 2B LW model B clear sky					Aqua 2B LW model B clear sky			
Type	<i>n</i>	Mean W m ^{−2}	Bias W m ^{−2} (%)	σ W m ^{−2} (%)	<i>n</i>	Mean W m ^{−2}	Bias W m ^{−2} (%)	σ W m ^{−2} (%)
Island	269	397.1	2.8 (0.7)	11.8 (3.0)	119	391.5	2.5 (0.6)	13.3 (3.4)
Coastal	810	278.7	−3.1 (−1.1)	13.3 (4.7)	506	282.4	−1.1 (−0.4)	13.2 (4.7)
Polar	794	145.2	−8.3 (−5.4)	15.0 (9.8)	1008	109.5	−9.0 (−7.6)	12.4 (10.4)
Continental	6822	291.8	−6.2 (−2.1)	12.7 (4.3)	3698	279.1	−8.2 (−2.8)	13.1 (4.6)
Desert	4391	314.3	−0.2 (−0.1)	20.7 (6.6)	1783	301.3	−3.0 (−1.0)	22.9 (7.5)
Global	13 086	291.8	−3.9 (−1.3)	16.5 (5.6)	7114	262.7	−6.3 (−2.3)	16.7 (6.2)

Terra 2B LW model B cloudy sky					Aqua 2B LW model B cloudy sky			
Type	<i>n</i>	Mean W m ^{−2}	Bias W m ^{−2} (%)	σ W m ^{−2} (%)	<i>n</i>	Mean W m ^{−2}	Bias W m ^{−2} (%)	σ W m ^{−2} (%)
Island	9471	417.9	5.7 (1.4)	14.3 (3.5)	5860	418.6	5.8 (1.4)	14.6 (3.5)
Coastal	3706	353.0	4.4 (1.3)	19.5 (5.6)	2411	349.5	2.7 (0.8)	19.2 (5.5)
Polar	36 641	215.9	−5.3 (−2.4)	28.1 (12.7)	22 270	213.4	−9.1 (−4.1)	27.8 (12.5)
Continental	19 938	324.0	−2.7 (−0.8)	20.5 (6.3)	13 116	318.4	−4.4 (−1.4)	21.5 (6.7)
Desert	5596	330.4	2.5 (0.7)	23.4 (7.1)	4245	340.0	9.2 (2.8)	29.9 (9.0)
Global	75 352	285.1	−2.2 (−0.8)	25.4 (8.9)	47 902	285.3	−3.8 (−1.3)	26.7 (9.2)

that surface albedo values derived from the ERBE clear-sky TOA data do not accurately represent the surface albedo values for polar regions further supports the conclusion that the Li and Garand (1994) surface albedo formulation, which is based on the ERBE clear-sky TOA data, should be updated to improve the accuracy of the SW downward fluxes derived from SW model A net fluxes.

In contrast to the implementation of a revised TOA albedo dataset, no perceptible differences in the *Terra* and *Aqua* SW flux calculations have been clearly associated with the other algorithm improvements: the replacement of the Geophysical Fluid Dynamics Laboratory aerosol optical depths (Haywood et al. 1999) in SW model A with the 550-nm Model of Atmospheric Transport Chemistry (MATCH) climatological aerosol optical depths (Collins et al. 2001), and the replacement of the ERBE-era four-class surface-type map in SW model B with a new surface map based on a 10-min land–water map and International Geosphere-Biosphere Programme (IGBP) surface classification.

b. LW models

Statistical comparisons between the CERES-derived and surface-measured downward LW fluxes are pre-

sented in Table 2 for both the *Terra* and *Aqua* orbital crossings over the 33 surface sites considered in this study. Percentage differences are provided in addition to the flux values for the systematic and random errors in Table 2 to gauge the relative importance of the flux values. As with the SW values, the comparisons between the CERES-derived and surface-measured fluxes are arranged by surface type: island, coastal, polar, continental, desert, and global, rather than by individual surface site. Graphical comparisons between the CERES-derived and surface-measured results are shown in Fig. 4 for the *Aqua* overpasses. The corresponding results for the *Terra* overpasses have not been presented since the *Terra* and *Aqua* comparisons are very similar for all the cases in this study.

Figure 4a and the top portion of Table 2 provide the clear-sky comparisons between LW model A and the surface-measured fluxes. Figure 4b shows the corresponding comparisons for the bin-averaged data, which reveals the overall relationship obscured by the sampling noise. The results in the top portion of Table 2 show small systematic errors, less than $\pm 5.5\ W\ m^{-2}$ for nearly all the surface types, with the notable exception of the polar cases where the negative systematic errors are of the order from -15 to $-11\ W\ m^{-2}$. Although the

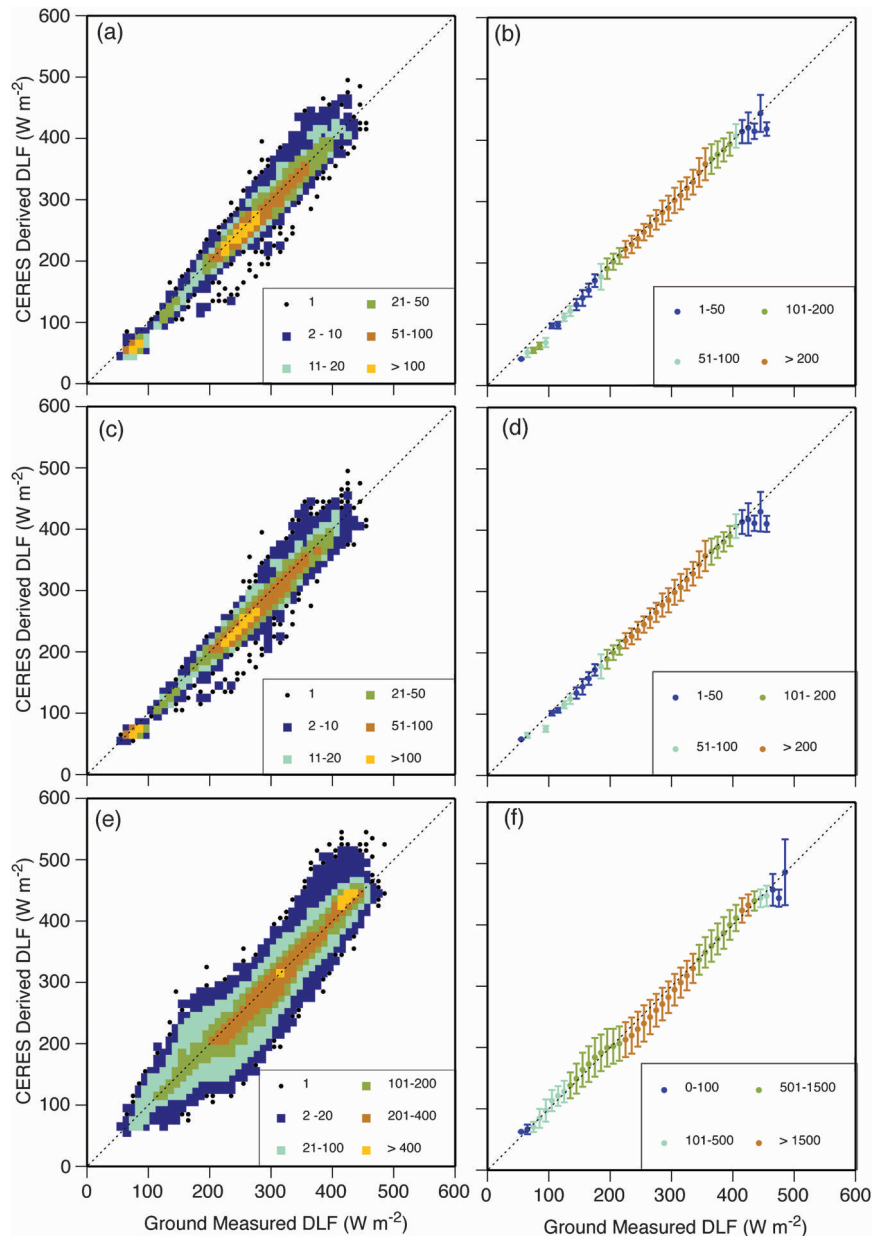


FIG. 4. Graphical comparisons between surface-measured fluxes and CERES-derived fluxes from *Aqua* measurements for (a),(b) LW model A under clear-sky conditions, (c),(d) LW model B under clear-sky conditions, and (e),(f) LW model B under cloudy-sky conditions for all the surface sites used in this study. The individual plots follow the same format as Fig. 2, but the bin sizes are 10 W m^{-2} .

magnitude of the systematic errors for the polar cases does not appear to be that large, the results in Table 2 reveal that average flux values for the polar cases are roughly 50%–75% less than those of the other cases. Thus, the magnitude of the systematic errors in relation to the fluxes for the polar cases is significantly greater than for the other cases, as revealed by the percentage differences in Table 2. Separately examining the plots of

the surface-type cases (not shown) further reveals that the polar cases are wholly responsible for the large negative systematic errors that appear in Fig. 4a for flux values less than 200 W m^{-2} . This significant underestimation of the downward LW surface flux for the polar cases is consistent with the results of Zhou et al. (2007), who demonstrated that formulas including a $\ln(w)$ term, such as Eq. (8) for LW model A, tend to underestimate

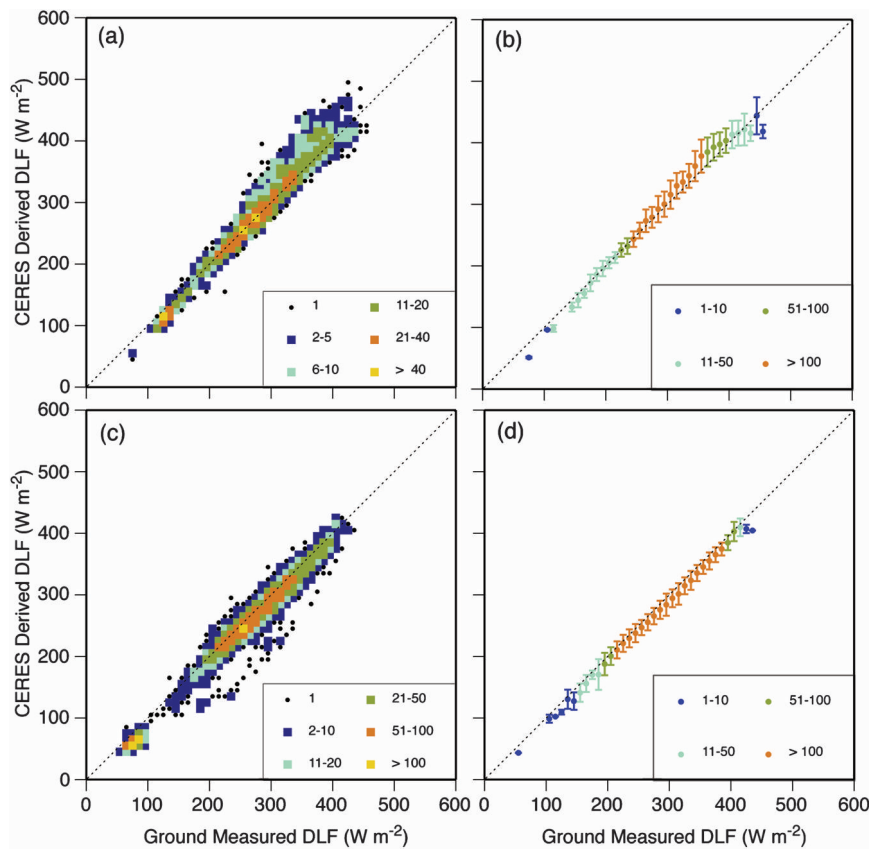


FIG. 5. Graphical comparisons between surface-measured fluxes and CERES-derived fluxes showing the differences between (a),(b) daytime and (c),(d) nighttime measurements from the *Aqua* spacecraft for LW model A under clear-sky conditions for all the surface sites used in this study. The individual plots follow the same format as Fig. 3, but the bin sizes are 10 W m^{-2} .

the downward LW flux significantly for low water vapor amounts (i.e., $w < 1 \text{ cm}$). The recommended solution by Zhou et al. (2007) was to reformulate the flux equations in terms of $\ln(1 + w)$, which would retain the logarithmic limit for large values of w but asymptote to the linear limit as w approaches zero.

The results in the top portion of Table 2 also show somewhat greater random error for the desert cases in comparison with the other surface types. This enhanced random error is associated with the overestimation of the fluxes above 350 W m^{-2} for the desert cases presented in Fig. 4a, and has been attributed to surface skin temperature values that exceed the lowest-layer air temperature to such an extent that the models retrieve unrealistically high near-surface air temperatures. An effective solution is to constrain the near-surface air temperature so that superadiabatic lapse rates cannot occur in the derivation of the lowest-layer air temperatures (GKSW). Such a code modification has been formulated for implementation into the next edition of the CERES processing.

The comparisons in Fig. 4a further reveal a modest number of cases where LW model A significantly underestimates the downward fluxes to the surface. Figure 5, which separates the results in Fig. 4a by day (Fig. 5a) and night (Fig. 5c), and the results in Fig. 4b by day (Fig. 5b) and night (Fig. 5d), shows that most of the flux underestimates occur during the night, a result similar to that observed by Gupta et al. (2004) for the CERES-TRMM data. The causes for the increased incidence of underestimates at night have been attributed to the inadequacy of the day–night temperature retrievals and the CERES cloud detection algorithm (Minnis et al. 2008) that uses both visible and infrared radiance techniques for daylight conditions, but only the infrared technique is available for nighttime conditions. Evidence suggests that low-altitude clouds over cool surfaces can easily be misidentified as clear skies if the infrared-only cloud algorithm is used, thereby resulting in an underestimation of the model-derived downward LW fluxes at the surface. As shown in the top portion of Table 3, the day–night difference for LW model A is of the order

TABLE 3. Comparisons between surface-measured fluxes and CERES-derived fluxes for LW model A under clear-sky conditions, LW model B under clear-sky conditions, and LW model B under cloudy-sky conditions for the global scene type separated between day and night. The column format is the same as Table 1.

<i>Terra</i> 2B LW model A clear sky					<i>Aqua</i> 2B LW model A clear sky			
Time	<i>n</i>	Mean $W \text{ m}^{-2}$	Bias $W \text{ m}^{-2}$ (%)	$\sigma W \text{ m}^{-2}$ (%)	<i>n</i>	Mean $W \text{ m}^{-2}$	Bias $W \text{ m}^{-2}$ (%)	$\sigma W \text{ m}^{-2}$ (%)
Day	6448	302.5	6.0 (2.0)	16.9 (5.7)	2447	291.2	6.0 (2.1)	19.0 (6.7)
Night	6573	287.7	−7.6 (−2.6)	13.6 (4.6)	4577	250.2	−9.9 (−3.8)	13.8 (5.3)
Day/night	13 021	295.0	−0.9 (−0.3)	16.9 (5.7)	7068	264.7	−4.4 (−1.6)	17.6 (6.5)

<i>Terra</i> 2B LW model B clear sky					<i>Aqua</i> 2B LW model B clear sky			
Time	<i>n</i>	Mean $W \text{ m}^{-2}$	Bias $W \text{ m}^{-2}$ (%)	$\sigma W \text{ m}^{-2}$ (%)	<i>n</i>	Mean $W \text{ m}^{-2}$	Bias $W \text{ m}^{-2}$ (%)	$\sigma W \text{ m}^{-2}$ (%)
Day	6476	296.7	0.3 (0.1)	17.6 (5.9)	2467	284.9	−0.1 (−0.1)	19.1 (6.7)
Night	6610	287.1	−8.1 (−2.7)	14.2 (4.8)	4603	250.5	−9.6 (−3.7)	13.9 (5.4)
Day/night	13 086	291.8	−3.9 (−1.3)	16.5 (5.6)	7114	262.7	−6.3 (−2.3)	16.7 (6.2)

<i>Terra</i> 2B LW model B cloudy sky					<i>Aqua</i> 2B LW model B cloudy sky			
Time	<i>n</i>	Mean $W \text{ m}^{-2}$	Bias $W \text{ m}^{-2}$ (%)	$\sigma W \text{ m}^{-2}$ (%)	<i>n</i>	Mean $W \text{ m}^{-2}$	Bias $W \text{ m}^{-2}$ (%)	$\sigma W \text{ m}^{-2}$ (%)
Day	34 168	309.5	3.0 (1.0)	20.3 (6.6)	22 436	307.8	1.9 (0.6)	23.1 (7.6)
Night	41 184	264.9	−6.5 (−2.4)	28.1 (10.4)	25 234	265.1	−8.8 (−3.2)	28.4 (10.4)
Day/night	75 352	285.1	−2.2 (−0.8)	25.4 (8.9)	47 902	285.3	−3.8 (−1.3)	26.7 (9.2)

13–16 $W \text{ m}^{-2}$ for the global fluxes. Not shown are the day–night flux differences for the various surface types, which have been found to follow a progression from: the desert cases where the day–night flux differences are over twice as large as the global values; to the polar and continental cases where the results are comparable in magnitude to the global values; to the coastal cases where very little day–night difference is seen; and finally the island cases that have a slightly opposite dependence from the global values. The large day–night flux differences for deserts have been attributed to the combined overestimation of the near-surface air temperature during the day and underestimation at night. For the coastal and island cases, where the diurnal variations in surface temperature are smallest, the small day–night differences indicate that these cases are affected the least by modeling problems.

Figures 4c and 4d and the middle portion of Table 2 provide the clear-sky comparisons between LW model B and the surface-measured fluxes. The results in the middle portion of Table 2 show small systematic errors, less than $\pm 9 W \text{ m}^{-2}$ for all surface types. The noticeable improvement in the polar cases has been achieved in LW model B, despite the use of a $\ln(w)$ term, by placing a lower bound of 0.3 kg m^{-2} on the total water vapor amount allowed by the model calculations, and by the serendipitous use of water vapor amounts in kg m^{-2} rather than g cm^{-2} which increased the numerical value of w by an order of magnitude, and thus, lowered the threshold where the model begins to severely underestimate the downward LW surface flux by an order of magnitude. Although not as elegant as the Zhou et al.

(2007) solution, these model differences do prevent the fluxes from falling to unrealistically low values. Nevertheless, since the average fluxes for the polar cases are roughly 50%–75% less than those of the other cases, the comparable flux biases are equivalent to significantly larger percentage biases. Thus, modifying the LW model B algorithm to use a $\ln(1 + w)$ term is warranted. As with LW model A, LW model B produces clear-sky results for the desert cases that have enhanced random errors caused by persistent overestimation of the clear-sky fluxes above $350 W \text{ m}^{-2}$. As before, the solution is to constrain the near-surface air temperature so that superadiabatic lapse rates cannot occur in the lowest layer of the atmosphere. GKSW used LW model B as a case study to analyze the near-surface air temperature issue and to derive viable solutions applicable not only to LW models B but also LW model A and the Zhou et al. (2007) parameterization.

Also apparent from Fig. 4c are the modest number of cases where LW model B significantly underestimates the downward fluxes to the surface with a pattern strikingly similar to that shown in Fig. 4a by LW model A. Figure 6, which separates the results in Fig. 4c by day (Fig. 6a) and night (Fig. 6c), and the results in Fig. 4d by day (Fig. 6b) and night (Fig. 6d), shows that most of the flux underestimates once again occur during the night, when the cloud detection techniques are least reliable. The day–night difference shown in the middle portion of Table 3 for LW model B is similar to that shown in the top portion of Table 3 for LW model A, with values of the order 8–10 $W \text{ m}^{-2}$ for the global fluxes. The day–night flux differences for all the surface types— island, coastal,

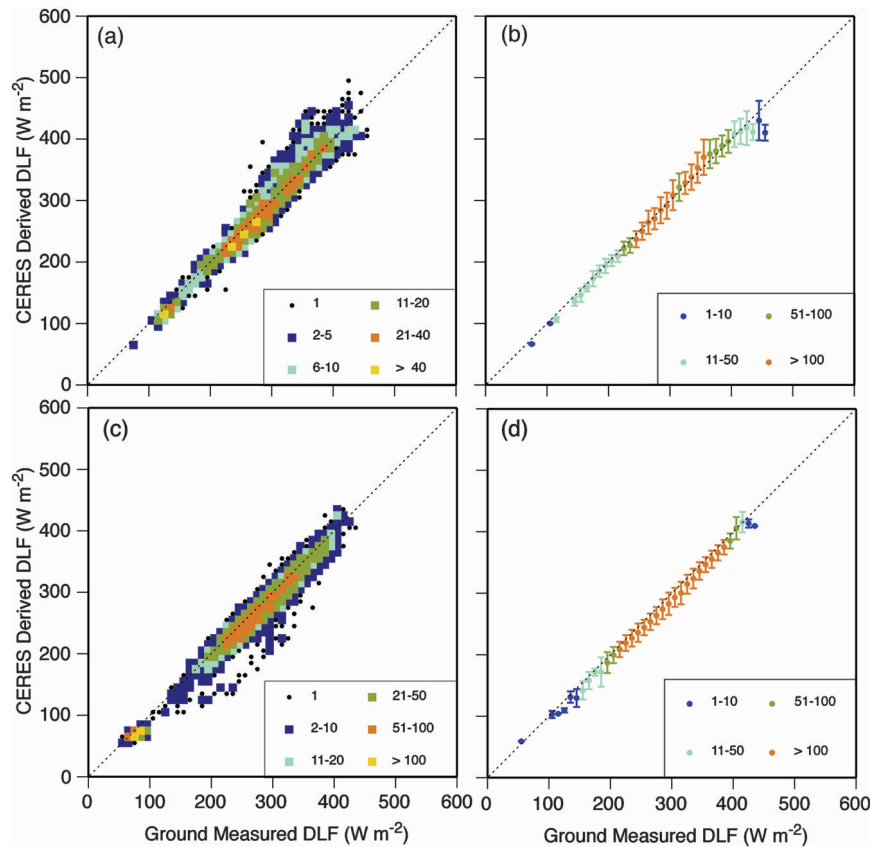


FIG. 6. Graphical comparisons between surface-measured fluxes and CERES-derived fluxes showing the differences between (a),(b) daytime and (c),(d) nighttime measurements from the *Aqua* spacecraft for LW model B under clear-sky conditions for all the surface sites used in this study. The individual plots follow the same format as Fig. 3, but the bin sizes are 10 W m^{-2} .

polar, continental, and desert—follow nearly the same patterns described for LW model A. Considering that LW models A and B were created from fundamentally very different formulations (Inamdar and Ramanathan 1997; Gupta 1989) yet produce very similar results lends further credence to the conclusion that the inadequacy in capturing the diurnal temperature cycle and the model inputs for the cloud amounts is responsible for the modest number of cases where the surface-measured fluxes are severely underestimated at night.

Figures 4e and 4f and the bottom portion of Table 2 provide the cloudy-sky comparisons between LW model B and the surface-measured fluxes. The results in the bottom portion of Table 2 show small systematic errors, less than or equal to $\pm 9.2 \text{ W m}^{-2}$ for all surface types, with most of these cloudy-sky biases being within 4 W m^{-2} of the clear-sky biases. The desert case for *Aqua*, however, produces a cloudy-sky bias that is 12.2 W m^{-2} greater than the clear-sky bias. This difference for the desert case has been attributed to the substantial number of observed overestimates in the near-surface air temperature. The

LW model B results in Table 2 also reveal that nearly every cloudy-sky case has a more positive bias than the associated clear-sky case, yet whether this is random chance or a true signal remains to be determined. In addition, although the LW model B clear-sky and cloudy-sky results produce comparable systematic errors in Table 2, the random errors for the cloudy-sky cases tend to be significantly larger, with the global cases being about 50% greater. Such an enhanced random error is consistent with the results from SW model B, where the added complexity of clouds decreases the precision of the surface flux retrievals. Of the various surface types, the polar sites tend to suffer the greatest increase in uncertainty due to the presence of clouds or the misidentification of snow as clouds. This is most noticeable between 150 and 300 W m^{-2} in Fig. 4e where the flux comparisons show an increased dispersion that is wholly associated with the cloudy-sky polar cases. The only notable change in LW model B between *Terra* and *Aqua* was a modification to handle clouds over high-altitude regions such as Tibet whenever cloud-base pressures

were unavailable. Since no surface measurements were available for those regions during the *Terra/Aqua* time frame, however, this modification has no effect on the results in the present study.

5. Summary and conclusions

Efforts have been undertaken since the beginning of the CERES/TRMM mission to validate the accuracy and precision of the downward SW and LW surface fluxes produced during the processing of the CERES single scanner footprint data (Gupta et al. 2004). With the end of the MODIS Collection-4 data production in July 2006, the CERES Edition 2B data processing was also concluded. This created an opportunity to assess the status of the surface-only flux algorithms for a complete and consistent multiyear data record associated with the CERES Edition 2B data that covers the 77-month period from March 2000 through July 2006 for *Terra* and the 46-month period from July 2002 through April 2006 for *Aqua*. The CERES processing uses two SW (Li et al. 1993b; Gupta et al. 2001) and two LW (Inamdar and Ramanathan 1997; Gupta 1989) models to calculate the surface fluxes from satellite-derived and ancillary input parameters that were provided by sources such as CERES (TOA radiances), MODIS (cloud parameters), GMAO (GEOS 4.0.3 meteorology), and NCEP-SMOBA (ozone products). The success criteria for these models were taken from Suttles and Ohring (1986) who estimated that surface flux retrievals from satellite measurements should have accuracies of $\pm 20 \text{ W m}^{-2}$ on an instantaneous footprint basis to be truly useful in climate research studies.

Clear-sky fluxes retrieved by SW model A (Li et al. 1993b) satisfy the established accuracy requirements for the global case; however, there is considerable scatter and the results for the individual surface types often exceed the established bias limits. Most pervasive are the significant underestimates of the downward surface fluxes for cases with very low water vapor amounts. This problem is most notable for the polar cases but is also visible in the low-flux continental cases. Evidence suggests that the most probable cause for these underestimates is an inadequacy in the Li and Garand (1994) albedo formulation. In addition, the desert cases, and only the desert cases, tend to underestimate the downward surface fluxes greater than 800 W m^{-2} . No specific cause for the underestimate in the desert case has been identified. Severe overestimates of the downward surface fluxes also occur occasionally, most notably for the island cases. These severe overestimates have been linked to underestimates of the cloudiness in the satellite retrievals from the imager data.

As with SW model A, SW model B (Gupta et al. 2001) also retrieves clear-sky surface fluxes that satisfy the established accuracy requirements for the global case. Unlike SW model A, however, SW model B nearly satisfies the validation criteria for the clear-sky cases for each of the surface types. Indeed, the large underestimates of the downward surface fluxes are absent for the polar cases as well as the desert cases exceeding 800 W m^{-2} . Nevertheless, the pattern of severe overestimates of the downward surface fluxes for the island cases is virtually identical to the results from SW model A, which further supports the conclusion that those particular overestimates are due to model inputs, rather than the parameterizations. Although SW model B retrieves cloudy-sky surface fluxes that satisfy the established accuracy requirements for the global case, there is considerable scatter and the results for the individual surface types often exceed the established bias limits. Similar results for cloudy-sky cases have been previously reported (Rossow and Zhang 1995; Gautier and Landsfeld 1997), which emphasize the difficulty of matching TOA and surface measurements for inhomogeneous cases, such as those involving clouds. The large random errors observed for the SW fluxes, however, are not entirely attributable to the CERES surface flux retrievals. Significant errors can also arise from the surface measurement process as well as the spatial and temporal variability of the insolation fields in the real world (Zelenka et al. 1999).

LW model A (Inamdar and Ramanathan 1997) provides very good clear-sky results, $\pm 5.4 \text{ W m}^{-2}$ (from -1.9 to 1.5%), for most surface types; however, the polar sites do yield a modest negative bias, from -15 to -11 W m^{-2} (from -13 to -7.2%), at low water vapor amounts. This flux underestimation could possibly be remedied by reformulating the nonwindow portion of the LW model A parameterization into terms dependent upon $\ln(1 + w)$, which would correctly handle the low water vapor amounts encountered for polar and high-altitude regions. Meanwhile, LW model B (Gupta 1989) provides good clear-sky and cloudy-sky results, $\pm 9.2 \text{ W m}^{-2}$ (from -7.6% to 2.8%), for all surface types. Despite the overall agreement both LW models A and B tend to overestimate the fluxes above 350 W m^{-2} for the desert cases. GKS found that applying a near-surface air temperature constraint would easily solve this discrepancy, and thus, have modified both codes to reflect this improvement for the next edition of the CERES processing. In addition, both LW models A and B tend to underestimate the surface fluxes for a modest number of nighttime cases; however, these particular discrepancies are caused by underestimates of the cloud amount input into the models, and thus, do not represent an inadequacy

in either parameterization. Even with the noted discrepancies, both LW models A and B produce surface fluxes that easily satisfy the instantaneous flux tolerances of $\pm 20 \text{ W m}^{-2}$ that were established for the CERES project.

While previous validation efforts have resulted in significant improvements to the surface-only flux algorithms, the present results suggest that further improvements are also necessary, especially with regard to the SW models. For instance, SW model A needs an improved surface albedo formulation, while SW model B needs the aerosol optical properties to be replaced with a more representative database. SW model B also needs to be reworked to reduce the large systematic difference between clear- and cloudy-sky cases.

Acknowledgments. ARM data have been made available through the U.S. Department of Energy as part of the Atmospheric Radiation Measurement Program. GMD data have been made available through NOAA's Earth System Research Laboratory/Global Monitoring Division–Radiation (G-RAD). SURFRAD data have been made available through NOAA's Air Resources Laboratory/Surface Radiation Research Branch. The authors thank D. A. Rutan (SSAI) for providing the CAVE database, and E. G. Dutton for making available the BSRN data. The authors also thank B. A. Wielicki, P. W. Stackhouse, G. G. Gibson, and the reviewers for providing valuable advice and suggestions regarding the manuscript. The authors acknowledge the guidance and leadership of the late W. L. Darnell, who formed the surface-only flux algorithm group within the CERES project. This research was supported through the NASA Science Mission Directorate as part of the CERES project.

REFERENCES

- Augustine, J. A., J. J. DeLuise, and C. N. Long, 2000: SURFRAD – A national surface radiation budget network for atmospheric research. *Bull. Amer. Meteor. Soc.*, **81**, 2341–2357.
- Barkstrom, B. R., E. F. Harrison, G. L. Smith, R. N. Green, J. F. Kibler, R. D. Cess, and ERBE Science Team, 1989: Earth Radiation Budget Experiment archival and April 1985 results. *Bull. Amer. Meteor. Soc.*, **70**, 1254–1262.
- Bloom, S., A. da Silva, and D. Dee, 2005: Documentation and validation of the Goddard Earth Observing System (GEOS) Data Assimilation System — version 4. NASA Tech. Rep. Series on Global Modeling and Data Assimilation, NASA/TM-2005-104606, 26 pp.
- Cess, R. D., and S. N. Tiwari, 1972: Infrared radiative energy transfer in gases. *Advances in Heat Transfer*, Vol. 8, J. P. Hartnett and T. F. Irvine Jr., Eds., Academic Press, 229–282.
- Charlock, T. P., and Coauthors, 1997: Compute surface and atmospheric fluxes (System 5.0). CERES Algorithm Theoretical Basis Doc. (ATBD Release 2.2), NASA/RP-1376, 84 pp.
- , F. G. Rose, D. A. Rutan, Z. Jin, and S. Kato, 2006: The global surface and atmospheric radiation budget: An assessment of accuracy with 5 years of calculations and observations. *Proc. 12th Conf. on Atmospheric Radiation*, Madison, WI, Amer. Meteor. Soc., 10.5. [Available online at <http://ams.confex.com/ams/pdfpapers/112984.pdf>.]
- Collins, W. D., P. J. Rasch, B. E. Eaton, B. V. Khattatov, J.-F. Lamarque, and C. S. Zender, 2001: Simulating aerosols using a chemical transport model with assimilation of satellite aerosol retrievals: Methodology for INDOEX. *J. Geophys. Res.*, **106**, 7313–7336.
- Darnell, W. L., W. F. Staylor, S. K. Gupta, and F. M. Denn, 1988: Estimation of surface insolation using Sun-synchronous satellite data. *J. Climate*, **1**, 820–835.
- , —, —, N. A. Ritchey, and A. C. Wilber, 1992: Seasonal variation of surface radiation budget derived from ISCCP-C1 data. *J. Geophys. Res.*, **97**, 15 741–15 760.
- Ellingson, R. G., J. S. Ellis, and S. B. Fels, 1991: The intercomparison of radiation codes used in climate models: Long-wave results. *J. Geophys. Res.*, **96**, 8929–8953.
- Gautier, C., and M. Landsfeld, 1997: Surface solar radiation flux and cloud radiative forcing for the Atmospheric Radiation Measurement (ARM) Southern Great Plains (SGP): A satellite, surface observations, and radiative transfer model study. *J. Atmos. Sci.*, **54**, 1289–1307.
- Gupta, S. K., 1989: A parameterization for longwave surface radiation from Sun-synchronous satellite data. *J. Climate*, **2**, 305–320.
- , W. L. Darnell, and A. C. Wilber, 1992: A parameterization for longwave surface radiation from satellite data: Recent improvements. *J. Appl. Meteor.*, **31**, 1361–1367.
- , A. C. Wilber, N. A. Ritchey, F. G. Rose, T. L. Alberta, T. P. Charlock, and L. H. Coleman, 1997: Regrid humidity and temperature fields (System 12.0). CERES Algorithm Theoretical Basis Doc. (ATBD Release 2.2), NASA/RP-1376, 20 pp.
- , D. P. Kratz, P. W. Stackhouse Jr., and A. C. Wilber, 2001: The Langley Parameterized Shortwave Algorithm (LPSA) for surface radiation budget studies (version 1.0). NASA/TP-2001-211272, 31 pp.
- , —, A. C. Wilber, and L. C. Nguyen, 2004: Validation of parameterized algorithms used to derive TRMM-CERES surface radiative fluxes. *J. Atmos. Oceanic Technol.*, **21**, 742–752.
- Haywood, J. M., V. Ramaswamy, and B. J. Soden, 1999: Tropospheric aerosol climate forcing in clear-sky satellite observations over the oceans. *Science*, **283**, 1299–1303.
- Inamdar, A. K., and V. Ramanathan, 1997: On monitoring the atmospheric greenhouse effect from space. *Tellus*, **49B**, 216–230.
- Jin, Z., T. P. Charlock, and C. K. Rutledge, 2002: Analysis of the broadband solar radiation and albedo over the ocean surface at COVE. *J. Atmos. Oceanic Technol.*, **19**, 1585–1601.
- Li, Z., and L. Garand, 1994: Estimation of surface albedo from space: A parameterization for global application. *J. Geophys. Res.*, **99**, 8335–8350.
- , H. G. Leighton, and R. D. Cess, 1993a: Surface net solar radiation estimated from satellite measurements: Comparisons with tower observations. *J. Climate*, **6**, 1764–1772.
- , —, K. Masuda, and T. Takashima, 1993b: Estimation of SW flux absorbed at the surface from TOA reflected flux. *J. Climate*, **6**, 317–330.
- Loeb, N. G., S. Kato, K. Loukachine, and N. Manalo-Smith, 2005: Angular distribution models for top-of-atmosphere radiative flux estimation from the Clouds and the Earth's Radiant Energy System instrument on the Terra satellite. Part I: Methodology. *J. Atmos. Oceanic Technol.*, **22**, 338–351.

- , —, —, —, and D. R. Doelling, 2007: Angular distribution models for top-of-atmosphere radiative flux estimation from the Clouds and the Earth's Radiant Energy System instrument on the *Terra* satellite. Part II: Validation. *J. Atmos. Oceanic Technol.*, **24**, 564–584.
- Masuda, K., H. G. Leighton, and Z. Li, 1995: A new parameterization for the determination of solar flux absorbed at the surface from satellite measurements. *J. Climate*, **8**, 1615–1629.
- Michalsky, J., E. Dutton, M. Rubes, D. Nelson, T. Stoffel, M. Wesley, M. Splitt, and J. DeLuisi, 1999: Optimal measurement of surface shortwave irradiance using current instrumentation. *J. Atmos. Oceanic Technol.*, **16**, 55–69.
- Minnis, P., and Coauthors, 1997: Cloud optical property retrieval (System 4.3). CERES Algorithm Theoretical Basis Doc. (ATBD Release 2.2), NASA/RP-1376, 60 pp.
- , and Coauthors, 2008: Cloud detection in nonpolar regions for CERES using TRMM VIRS and *Terra* and *Aqua* MODIS data. *IEEE Trans. Geosci. Remote Sens.*, **46**, 3857–3884.
- Moser, W., and E. Raschke, 1984: Incident solar radiation over Europe estimated from METEOSAT data. *J. Climate Appl. Meteor.*, **23**, 166–170.
- Ohmura, A., and Coauthors, 1998: Baseline Surface Radiation Network (BSRN/WCRP): New precision radiometry for climate change research. *Bull. Amer. Meteor. Soc.*, **79**, 2115–2136.
- Peixoto, J. P., and A. H. Oort, 1993: *Physics of Climate*. American Institute of Physics, 520 pp.
- Philipona, R., 2002: Underestimation of solar global and diffuse radiation measured at Earth's surface. *J. Geophys. Res.*, **107**, 4654, doi:10.1029/2002JD002396.
- Rossow, W. B., and Y.-C. Zhang, 1995: Calculation of surface and top of atmosphere radiative fluxes from physical quantities based on ISCCP data sets 2. Validation and first results. *J. Geophys. Res.*, **100**, 1167–1197.
- , and R. A. Schiffer, 1999: Advances in understanding clouds from ISCCP. *Bull. Amer. Meteor. Soc.*, **80**, 2261–2287.
- Rutan, D. A., F. G. Rose, N. M. Smith, and T. P. Charlock, 2001: Validation data set for CERES surface and atmospheric radiation budget (SARB). *WCRP/GEWEX News*, No. 1, International GEWEX Project Office, Silver Spring, MD, 11–12.
- Salomonson, V. V., W. L. Barnes, P. W. Maymon, H. E. Montgomery, and H. Ostrow, 1989: MODIS—Advanced facility instrument for studies of the Earth as a system. *IEEE Trans. Geosci. Remote Sens.*, **27**, 145–153.
- Stokes, G. M., and S. E. Schwartz, 1994: The Atmospheric Radiation Measurement (ARM) program: Programmatic background and design of the cloud and radiation testbed. *Bull. Amer. Meteor. Soc.*, **75**, 1201–1221.
- Suttles, J. T., and G. Ohring, 1986: Surface radiation budget for climate applications. NASA Reference Publication 1169, Washington, DC, 132 pp.
- Wielicki, B. A., B. R. Barkstrom, E. F. Harrison, R. B. Lee III, G. L. Smith, and J. E. Cooper, 1996: Clouds and the Earth's Radiant Energy System (CERES): An Earth Observing System experiment. *Bull. Amer. Meteor. Soc.*, **77**, 853–868.
- Wilber, A. C., D. P. Kratz, and S. K. Gupta, 1999: Surface emissivity maps for use in satellite retrievals of longwave radiation. NASA/TP-1999-209362, 35 pp.
- Yang, S. K., S. Zhou, and A. J. Miller, 1997: SMOBA: A 3-dimensional daily ozone analysis using SBUV/2 and TOVS measurements. NOAA rep. [Available online at http://www.cpc.noaa.gov/products/stratosphere/SMOBA/smoba_doc.shtml.]
- Young, D. F., P. Minnis, D. R. Doelling, G. G. Gibson, and T. Wong, 1998: Temporal interpolation methods for the Clouds and the Earth's Radiant Energy System (CERES) experiment. *J. Appl. Meteor.*, **37**, 572–590.
- Zelenka, A., R. Perez, R. Seals, and D. Renne, 1999: Effective accuracy of satellite-derived hourly irradiances. *Theor. Appl. Climatol.*, **62**, 199–207.
- Zhou, Y., D. P. Kratz, A. C. Wilber, S. K. Gupta, and R. D. Cess, 2007: An improved algorithm for retrieving surface downwelling longwave radiation from satellite measurements. *J. Geophys. Res.*, **112**, D15102, doi:10.1029/2006JD008159.